J Solid State Electrochem (2012) 16:3011–3025
DOI 10.1007/s10008-012-1739-y

ORIGINAL PAPER

Study of lithium ion intercalation/de-intercalation into $LiNi_{1/3}Mn_{1/3}Co_{1/3}O_2$ in aqueous solution using electrochemical impedance spectroscopy

K. C. Mahesh · H. Manjunatha · T. V. Venkatesha · G. S. Suresh

Received: 20 August 2011 / Revised: 30 August 2011 / Accepted: 28 March 2012 / Published online: 18 April 2012

Abstract The mechanism of lithium ion intercalation/de-intercalation into $LiNi_{1/3}Mn_{1/3}Co_{1/3}O_2$ cathode material prepared by reactions under autogenic pressure at elevated temperatures method is investigated both in aqueous and non-aqueous electrolytes using electrochemical impedance spectroscopy (EIS) technique. In accordance with the results obtained an equivalent circuit is used to fit the impedance spectra. The kinetic parameters of intercalation/de-intercalation processes are evaluated with the help of the same equivalent circuit. The dependence of charge transfer resistance (R_{ct}), exchange current (I_0), double layer capacitance (C_{dl}), Warburg resistance (Z_w), and chemical diffusion coefficient (D_{Li+}) on potential during intercalation/de-intercalation is studied. The behavior of EIS spectra and its potential dependence is studied to get the kinetics of the mechanism of intercalation/de-intercalation processes, which cannot be obtained from the usual electrochemical studies like cyclic voltammetry. The results indicate that intercalation and de-intercalation of lithium ions in aqueous solution follows almost similar mechanism in non-aqueous system. D_{Li+} values are in the range of 10^{-8} to 10^{-14} cm^2 s^{-1} in aqueous 5 M $LiNO_3$ and that in non-aqueous 1 M $LiAsF_6$/EC+DMC electrolyte is in the order of 10^{-12} cm^2 s^{-1} during the intercalation/de-intercalation processes. A typical cell $LiTi_2(PO4)_3$/5 M $LiNO_3$/$LiNi_{1/3}Mn_{1/3}Co_{1/3}O_2$ is constructed and the cycling stability is compared to that with an organic electrolyte.

Keywords Li-ion batteries · Lithium insertion/de-insertion reaction · EIS technique · Chemical diffusion coefficient · Kinetic parameters

K. C. Mahesh · H. Manjunatha · G. S. Suresh (✉)
Chemistry Research Centre, S. S. M. R. V. Degree College, Jayanagar
Bangalore 560041, India
e-mail: sureshssmrv@yahoo.co.in

T. V. Venkatesha
Department of Chemistry, Kuvempu University, Jnanasahyadri, Shankaraghatta
577451, Shimoga, India

Introduction

Aqueous rechargeable lithium ion batteries proposed by Dahn and co-workers have been of great interest not only for basic studies but also for applications [1]. In comparison with cells containing organic electrolytes, rechargeable lithium ion batteries with aqueous electrolytes have many advantages such as low cost, intrinsic safety, and environmental friendliness. Moreover the conductivity of inorganic electrolytes is typically two orders of magnitude larger than that of a non-aqueous system, which can satisfy the high rate capacity and specific power requirements [2]. Since the stability window of aqueous electrolytes is much smaller than that of non-aqueous solutions, the selection of intercalation materials is a key factor for the performance of the aqueous lithium battery cell [3]. $LiCoO_2$ has been used as a major cathode material for lithium-ion batteries since it was introduced by Sony Corporation [4]. Obviously, it is an excellent cathode material with low irreversible capacity loss and good cycling performance. However, its extensive application is limited owing to various factors such as expensiveness and toxicity of cobalt and limited number of lithium ions in the crystal structure of $LiCoO_2$. These drawbacks of $LiCoO_2$ accelerate intensive study to find an alternative cathode material for lithium-ion batteries.

The layer-structured $LiNi_{1/3}Mn_{1/3}Co_{1/3}O_2$ has shown to be the most promising alternative material for $LiCoO_2$ in

terms of operating voltage, capacity, cycleability, thermal stability, and material cost [5]. $LiNi_{1/3}Mn_{1/3}Co_{1/3}O_2$, which can be considered as a compound among Li-[NiCoMn]-O_2 series, was first proposed by Ozhuku and Makimura [5]. Thereafter many attempts have been made to study the possibilities of using this oxide with hexagonal structure, as cathode material in rechargeable lithium ion batteries [6–9]. This compound was synthesized either by traditional solid state or solution methods [10–12]. However, solid state reaction method requires prolonged heating at relatively high temperature with repeated intermediate grinding because of the heterogeneity of the precursors. Even though, solution methods lead to homogeneous materials with small particle size, the complex synthetic routes and the expensive reagents make these methods not fit for the industrial-scale production. These problems may be conquered in two ways: one is to alter the starting materials or heating conditions, and the other is to employ other synthesis methods [13].

Many techniques such as potentiostatic or galvanostatic pulse measurements have been used to understand the electrochemical behavior of the lithium-ion intercalation/deintercalation processes in the layered structure. However, ac measurements like electrochemical impedance spectroscopy (EIS) are found to be more informative [14–20]. In principle,

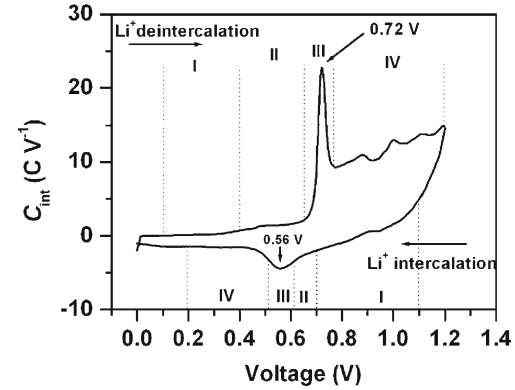

Fig. 2 Plot of intercalation capacitance, C_{int} vs. potential, E, of the $LiNi_{1/3}Mn_{1/3}Co_{1/3}O_2$ layered phase obtained by SSCV in 5 M $LiNO_3$ solution with a scan rate of 0.05 mV s^{-1} vs. SCE

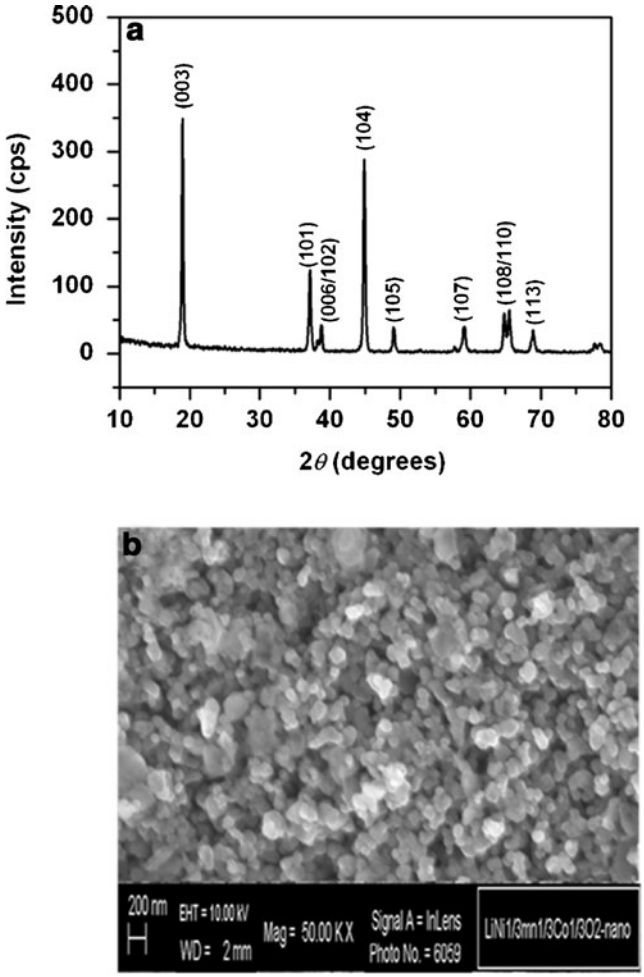

Fig. 1 XRD pattern of $LiNi_{1/3}Mn_{1/3}Co_{1/3}O_2$ synthesized by RAPET method

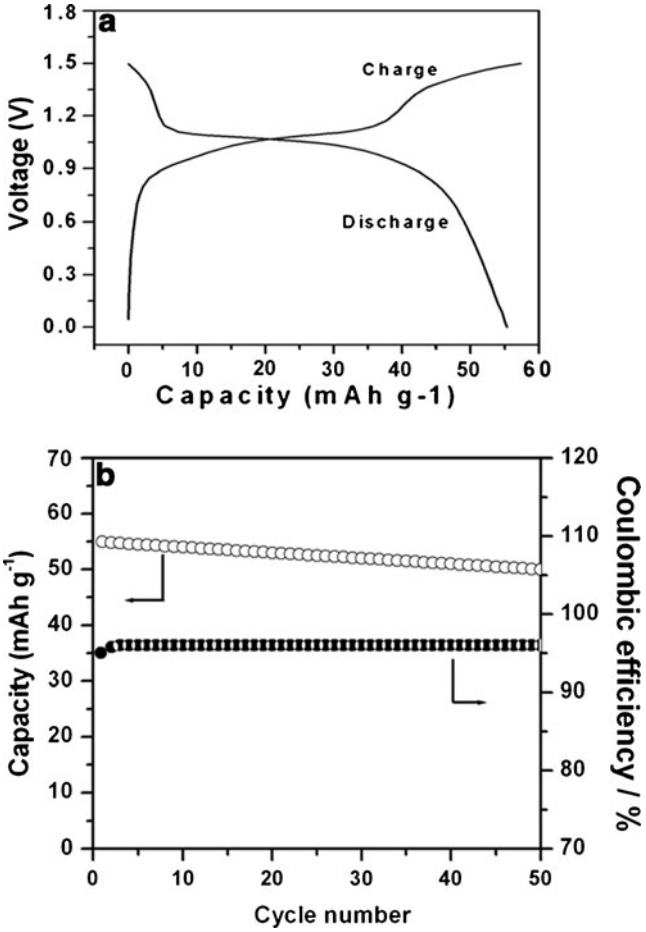

Fig. 3 **a** Charge–discharge curves **b** cycling stability and coulombic efficiency curves of $LiTi2(PO_4)_3$/5 M $LiNO_3$/$LiNi_{1/3}Mn_{1/3}Co_{1/3}O_2$ cell at the current density of 0.1 mA cm^{-2}

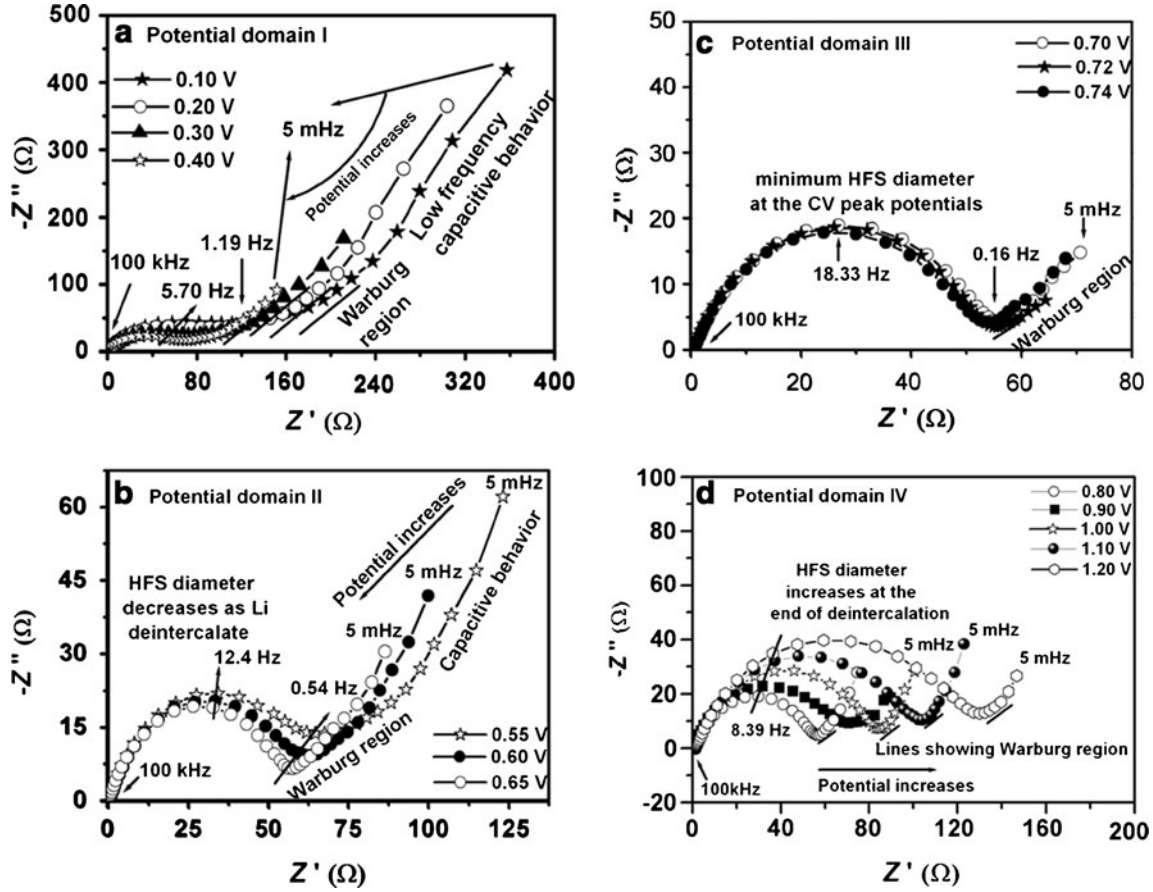

Fig. 4 Nyquist plots of the $LiNi_{1/3}Mn_{1/3}Co_{1/3}O_2$ electrode in 5 M $LiNO_3$ solution at different charge voltages

pulse and ac measurements contain the same information, but in practice, ac measurements offer several important advantages over pulse techniques [21]. The impedance measurements involve excitation of the electrochemical cell by an ac voltage of small amplitude (5 or 10 mV) and evaluation of the resistive and the reactive components, or other related parameters such as modulus of impedance and phase angle. Further, ac impedance measurements can be used to evaluate various parameters of the electrode material and the kinetics of the associated reactions. An electrode system comprises resistive, capacitive, and inductive components. The resistive component originates from the current collectors, electrolyte, bulk of the electrode materials, electron-transfer reaction at the electrode-electrolyte interfaces, etc. The capacitive component is due to the double layer charging. Inductive components are usually arising from the porous nature of the electrodes. The measured total impedance is comprised of the resistive and the reactive components of the individual processes, which may be represented by an appropriate analogue known as an electrical equivalent circuit [22]. Several attempts have been made to explain the impedance response of the intercalation materials of lithium ion batteries, such as graphite [17], $LiMn_2O_4$ [23], and $LiCoO_2$ [24]. Recently, we

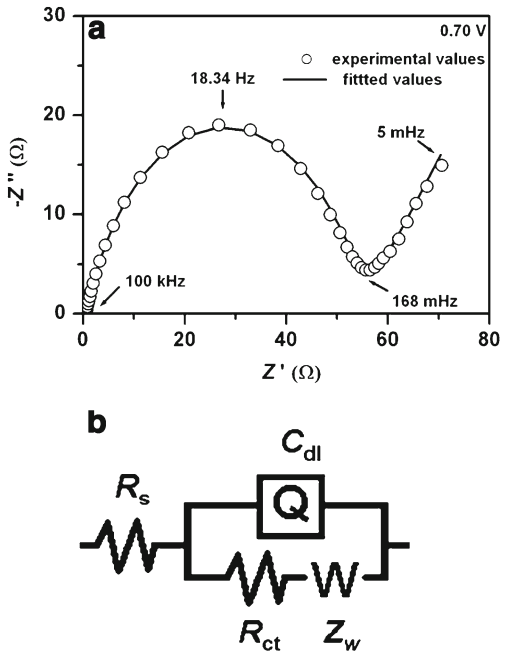

Fig. 5 **a** Experimental Nyquist plots $LiNi_{1/3}Mn_{1/3}Co_{1/3}O_2$ during charge and simulated result obtained. **b** The equivalent circuit used to simulate the experimental data

Table 1 Evaluated impedance parameters according to the equivalent circuit in Fig. 5b as a function of electrode potential during charge process

E (V)	R_s (Ω)	R_{ct} (Ω)	$(I_o/10^{-4})$ (A)	C_{dl} (mF)	Z_w (Ω)	$(D_{Li+}/10^{-10})$/ $cm^2\ s^{-1}$	$\log[(D_{Li+}/10^{-10})/cm^2\ s^{-1}]$
0.10	0.583	111.38	2.31	0.501	0.012	6.380	−6.195
0.20	0.575	91.26	2.82	0.522	0.014	0.508	−7.294
0.30	0.570	71.98	3.57	0.527	0.026	0.368	−7.433
0.40	0.569	70.64	3.64	0.511	0.044	0.256	−7.591
0.55	0.567	67.68	3.80	0.503	0.064	0.290	−7.537
0.60	0.564	62.91	4.09	0.501	0.094	0.018	−8.747
0.65	0.567	57.72	4.45	0.500	0.128	7.69×10^{-4}	−10.114
0.70	0.575	56.52	4.55	0.529	0.251	1.99×10^{-4}	−13.700
0.72	0.576	55.82	4.60	0.595	0.430	7.50×10^{-4}	−13.124
0.74	0.562	54.72	4.70	0.721	0.272	6.70×10^{-4}	−13.174
0.80	0.585	57.11	4.50	0.828	0.205	1.77×10^{-4}	−10.752
0.90	0.598	70.98	3.62	1.004	0.141	3.87×10^{-4}	−10.412
1.00	0.607	85.51	3.01	1.116	0.089	0.006	−9.231
1.10	0.607	104.36	2.46	1.147	0.044	0.315	−7.501
1.20	0.632	130.07	1.98	1.168	0.020	1.300	−6.886

have reported the kinetic studies of lithium ion insertion/de-insertion into the spinel $LiMn_2O_4$ from 2 M Li_2SO_4 aqueous solution using EIS technique [25].

$LiNi_{1/3}Mn_{1/3}Co_{1/3}O_2$ has been used as a cathode material in constructing aqueous rechargeable lithium batteries [26, 27]. However, in both the above works, authors have either

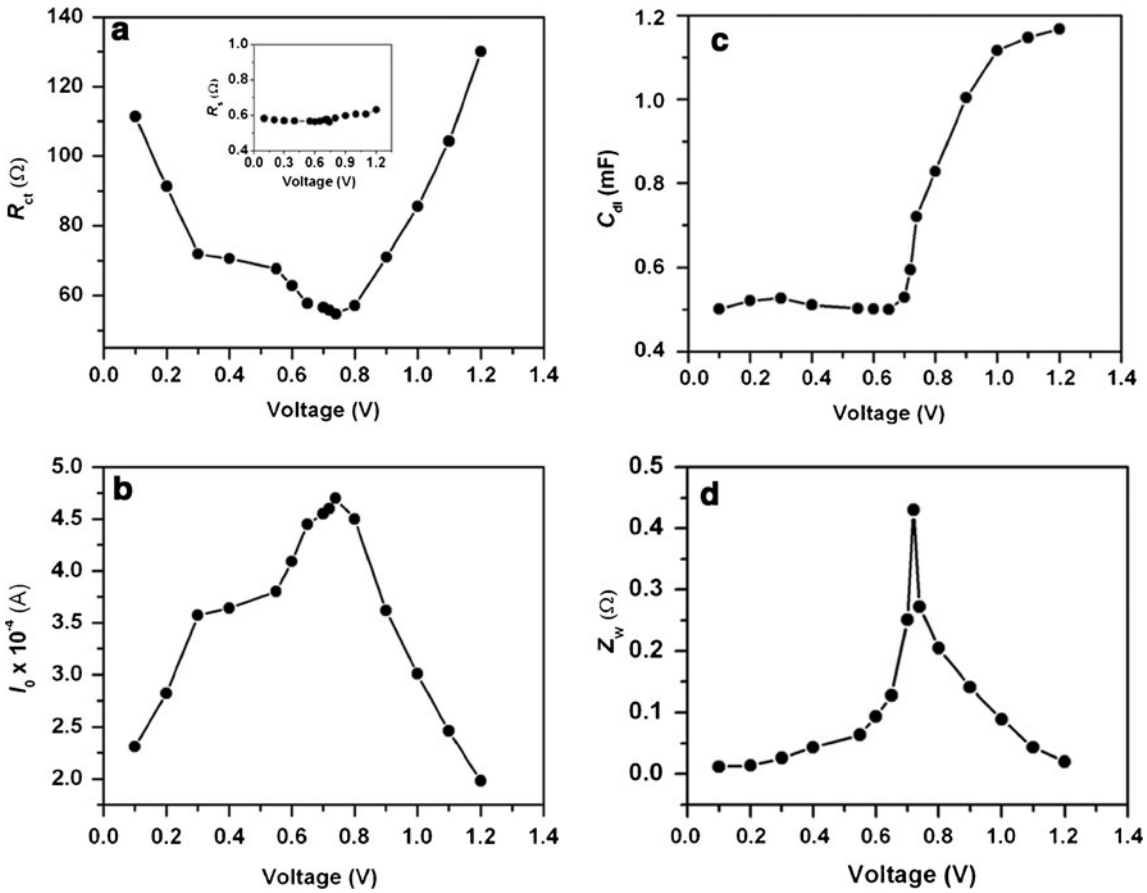

Fig. 6 Relationship between kinetic parameters and charge voltage in 5 M $LiNO_3$ solution

used commercial samples or the material synthesized by solid state method and constructed aqueous rechargeable lithium batteries, using polyaniline coated $Li_xV_2O_5$ and LiV_3O_8 as anode materials, respectively. It is evident that the electrochemical lithium intercalation reaction in aqueous electrolytes can be made possible by selecting suitable transition metal oxides and electrolytes. As discussed in the earlier section of this introductory part, aqueous rechargeable lithium batteries can compete with lead acid or Ni–Cd cells owing to the high conductivity of aqueous electrolytes promising high rate capability and relatively high energy and power densities. In this work, we report the synthesis of $LiNi_{1/3}Mn_{1/3}Co_{1/3}O_2$ by a simple heating method called reactions under autogenic pressure at elevated temperature (RAPET) method employing the use of a stainless steel cell. This method is good in controlling particle size and morphology at lower reaction temperature. The synthesis procedure is time and energy saving, and thus is promising for commercial application. The mechanism of intercalation–de-intercalation processes in $LiNi_{1/3}Mn_{1/3}Co_{1/3}O_2$ from aqueous and organic solutions is studied by evaluating the kinetic parameters such as chemical diffusion coefficient, charge transfer resistance, double layer capacitance, exchange current, etc., using EIS. The characteristic impedance structure of the spectra and its potential dependence provides important kinetic information on the mechanism of intercalation processes, which cannot be obtained from the usual electrochemical studies like cyclic voltammetry. The main objective is to rationalize, at least qualitatively, the potential dependence of the above mentioned kinetic parameters observed for lithium ion interaction/de-intercalation in the $LiNi_{1/3}Mn_{1/3}Co_{1/3}O_2$ layered phase in aqueous and non-aqueous electrolytes.

Experimental

Stoichiometric amounts of LiOH, MnO_2, $NiCO_3$, and Co $(OH)_2$ (all from Sigma Aldrich) are mixed and ground well. The mixture is introduced into a 5-ml Swagelok cell. The Swagelok parts consist of a small threaded tube closed by two caps from both sides. The filled Swagelok is closed tightly in oxygen environment and placed inside an alumina pipe in the middle of the programmable furnace. The temperature is raised at a rate of 10 °C/min to 600 °C and held at this temperature for 10 h. The chemical dissociation and transformation reaction takes place under the autogenic pressure of the precursor at the fixed temperature. The Swagelok cell is allowed to cool gradually to room temperature, opened and the obtained products are used after grinding.

Powder X-ray diffraction (XRD) patterns of the samples were recorded using a Philips X'pert Pro diffractometer with CuKα (λ=1.5418 Å) as the source. Electrodes were prepared by using stainless steel mesh as a current collector. The mesh was cut into circular shape of about 1 cm^2 area and welded with stainless steel wire for electrical contact. The mesh was sandblasted to remove the oxide layer, washed with water, rinsed with acetone, dried, and weighed. Powder mixture of the sample, carbon black, and polytetrafluoroethylene (PTFE) in the weight ratio 80:10:10 were ground in a mortar; a few drops of NMP were added to get slurry. It was coated onto the pretreated mesh and dried in a vacuum oven at 110 °C overnight. A three electrode electrochemical cell was employed for cyclic voltammetry (CV) in aqueous 5 M $LiNO_3$ solution. A saturated calomel electrode (SCE) and Pt foil were used as reference and counter electrodes, respectively. Electrochemical impedance measurements were carried out potentiometrically using a three electrode system with an ac excitation signal of 10 mV over the frequency range 100 kHz to 5 mHz. All the electrochemical measurements were made using the Biologic potentiostat–galvanostat instrument. All the experiments of $LiNi1_{/3}Mn_{1/3}Co_{1/3}O_2$ in organic electrolyte were carried out in the same way. The test cell was prepared with Li metal foil as reference and counter electrodes, and a 1-M $LiAsF_6$ dissolved in EC+DMC (1:1 *v*/*v*) as the electrolyte solution. Celgard 2400 was used as the separator. Assembling of the cell was carried out in a glove box filled with argon gas. All

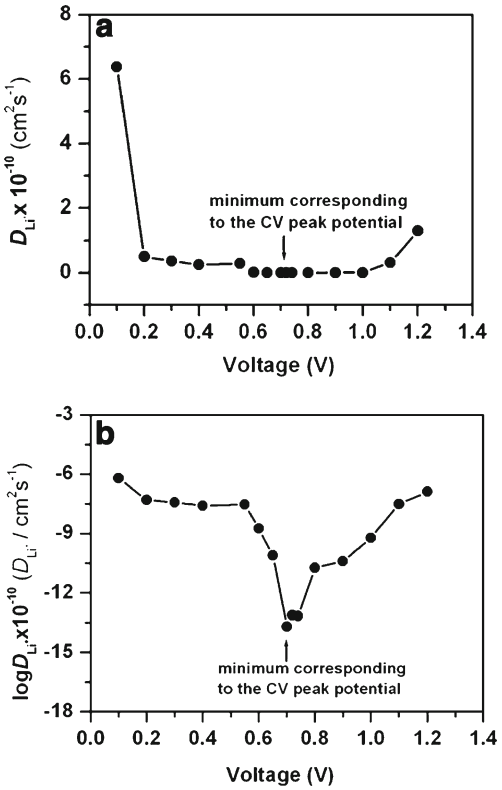

Fig. 7 Plots of **a** D_{Li+} and **b** log D_{Li+} against charge voltage in 5 M $LiNO_3$ solution

electrochemical measurements were performed at ambient temperature.

Results and discussion

Figure 1a shows the XRD pattern of $LiNi_{1/3}Mn_{1/3}Co_{1/3}O_2$ synthesized by RAPET method. The observed diffraction lines agree well with the XRD patterns reported in the literature for the same compound. $LiNi_{1/3}Mn_{1/3}Co_{1/3}O_2$ has a rhombohedral structure belonging to the *R3m* space group of a hexagonal –$NaFeO_2$ structure. In this solid solution, the valence states of Ni, Mn, and Co are 2+, 4+, and 3+, respectively. The low values of *R* factor, $R=(I_{102}+I_{006})/I_{101}$, relates to the integrated intensities of the corresponding well resolved peaks of the material confirm their hexagonal ordering. Highly resolved splitting of 006/102 and 108/110 peaks provide an evidence of a characteristic well-ordered layered structure of the compound. The ratios of the intensities of 003 and 104 peaks in the XRD pattern was found to be >1. This may indicate no pronounced cation mixing and thereby the electrochemical activity of these cathode materials in terms of capacity and rates of lithium ion de-insertion/insertion is supposed to be very good. We conclude from this XRD results that there are no remarkable impurities in the material obtained. Figure 1b shows the scanning electron microscope image of $LiNi_{1/3}Mn_{1/3}Co_{1/3}O_2$ synthesized by RAPET method. The well-dispersed crystalline particles are observed. The particles are non-spherical in shape having size less than 200 nm.

Figure 2 shows the plot of intercalation capacitance, C_{int}, versus potential for lithium ion intercalation/de-intercalation into the $LiNi_{1/3}Mn_{1/3}Co_{1/3}O_2$ layered phase obtained from CV profile in 5 M $LiNO_3$ aqueous solution between 0.0 and 1.2 V vs SCE. $LiNi_{1/3}Mn_{1/3}Co_{1/3}O_2$ exhibits sharp intense anodic peak centered at 0.72 V which corresponds to the de-intercalation of lithium ions and a cathodic peak at 0.56 V which corresponds to the lithium ion intercalation in accordance with the following equations.

$$\text{De}-\text{intercalation}: LiNi_{1/3}Mn_{1/3}Co_{1/3}O_2 \rightarrow Li_{(1-x)}Ni_{1/3}Mn_{1/3}Co_{1/3}O_2 + xLi^+ + xe^- \quad (1)$$

$$\text{Intercalation}: Li_{(1-x)}Ni_{1/3}Mn_{1/3}Co_{1/3}O_2 + xLi^+ + xe^- \rightarrow LiNi_{1/3}Mn_{1/3}Co_{1/3}O_2 \quad (2)$$

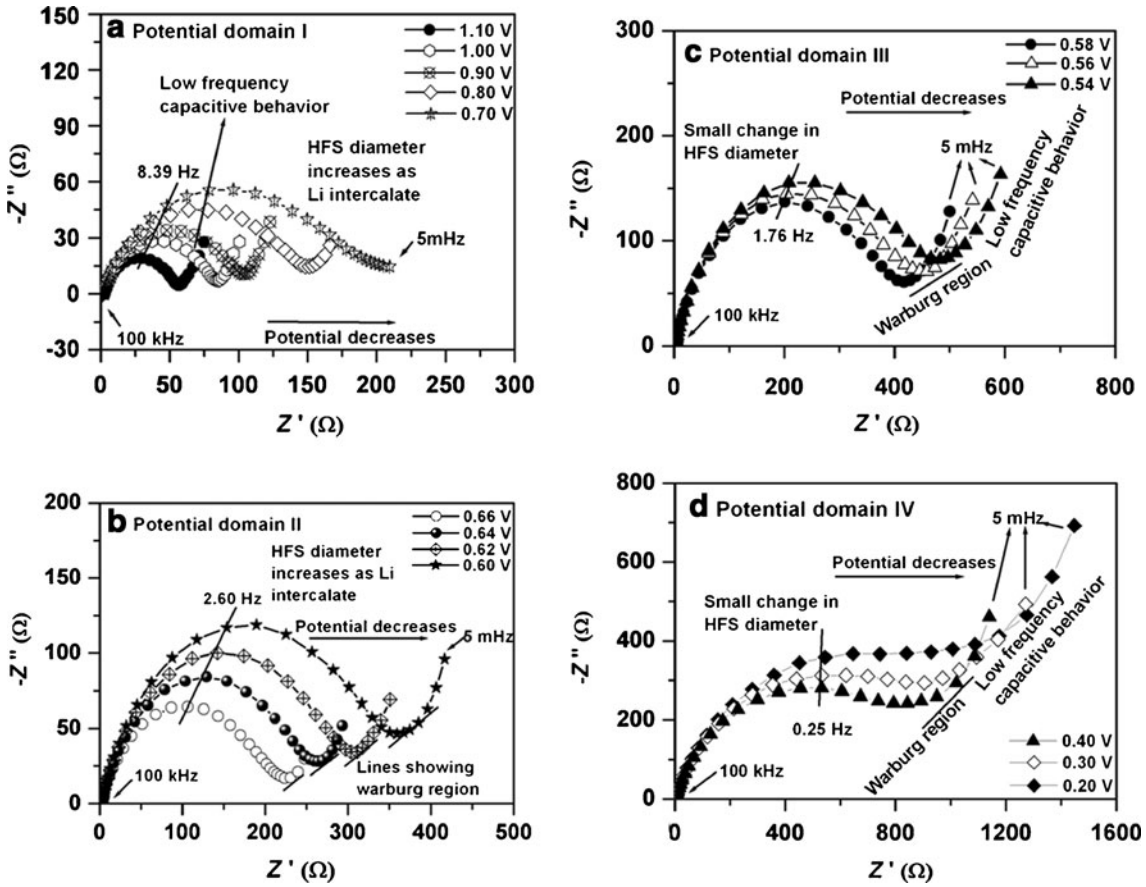

Fig. 8 Nyquist plots of the $LiNi_{1/3}Mn_{1/3}Co_{1/3}O_2$ electrode in 5 M $LiNO_3$ solution at different discharge voltages

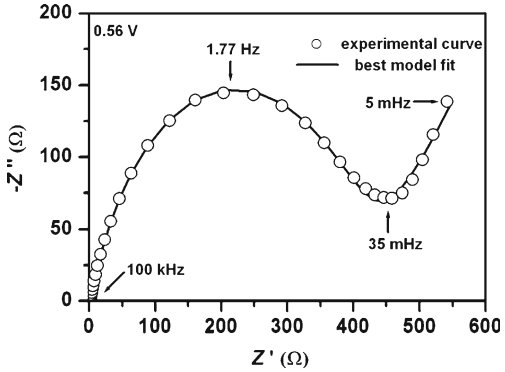

Fig. 9 Experimental Nyquist plots of $LiNi_{1/3}Mn_{1/3}Co_{1/3}O_2$ in 5 M $LiNO_3$ during discharge and simulated result obtained using the equivalent circuit in Fig. 5b

The entire potential range shown in Fig. 2 during de-intercalation can be divided into four domains: potential domain I relate to the region before the de-intercalation of lithium ions, potential domain II characterizes the beginning of de-intercalation, III refers to the vicinity of the peak and IV depicts the maximum delithiated $Li_{(1-x)}Ni_{1/3}Mn_{1/3}Co_{1/3}O_2$ phase according to Eq. (1). Similarly the potential range during intercalation can also be divided into four domains: potential domain I relate to the region before intercalation, II characterizes the potential domain at the beginning of intercalation into the layered phase. Domain III relate to the region of the CV peak and IV corresponds to the fully intercalated state in accordance with the Eq. (2).

To study the charge–discharge cycling behavior of the prepared $LiNi_{1/3}Mn_{1/3}Co_{1/3}O_2$ electrode, an electrochemical cell was costructed using $LiNi_{1/3}Mn_{1/3}Co_{1/3}O_2$ as cathode and $LiTi_2(PO_4)_3$ as anode in 5 M $LiNO_3$ aqueous solution. Figure 3a shows the typical charge–discharge curves of $LiTi_2(PO_4)_3$/5 M $LiNO_3$/$LiNi_{1/3}Mn_{1/3}Co_{1/3}O_2$ cell at the current density 0.1 mA cm^{-2} in the potential range 0 to 1.5 V. It is clear that during charge process lithium ions de-intercalate from $LiNi_{1/3}Mn_{1/3}Co_{1/3}O_2$ and intercalate into $LiTi_2(PO_4)_3$. The reverse process occurs during discharge process. These curves display a voltage plateau at about 1.0 V. Figure 3b shows the variation of discharge capacity and coulombic efficiency with cycle number. The cycling behavior of the cell shows that this kind of cell is good in reversible intercalation and de-intercalation of lithium ions.

Figure 4 shows a family of Nyquist plots related to lithium ion de-intercalation from $LiNi_{1/3}Mn_{1/3}Co_{1/3}O_2$ electrode in 5 M $LiNO_3$ solution in the potential range 0 to

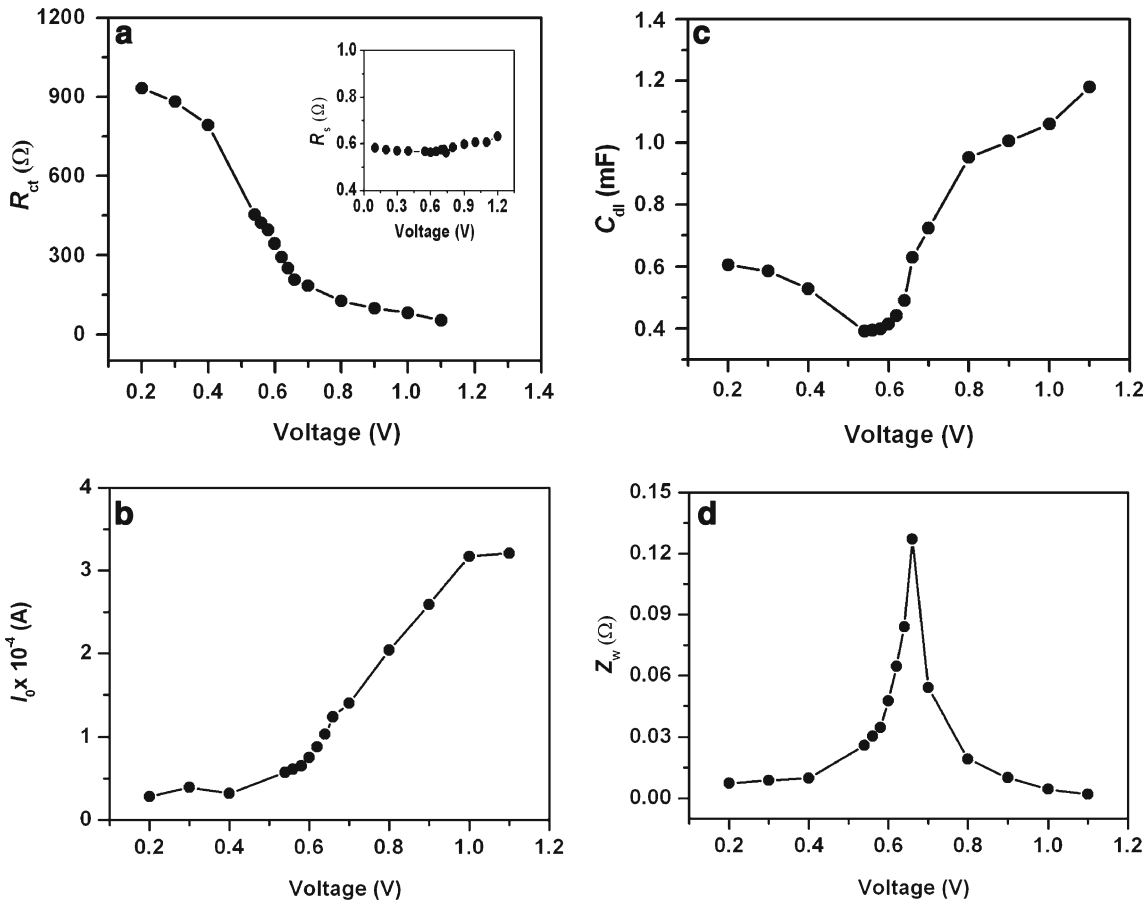

Fig. 10 Relationship between kinetic parameters and discharge voltage in 5 M $LiNO_3$ solution

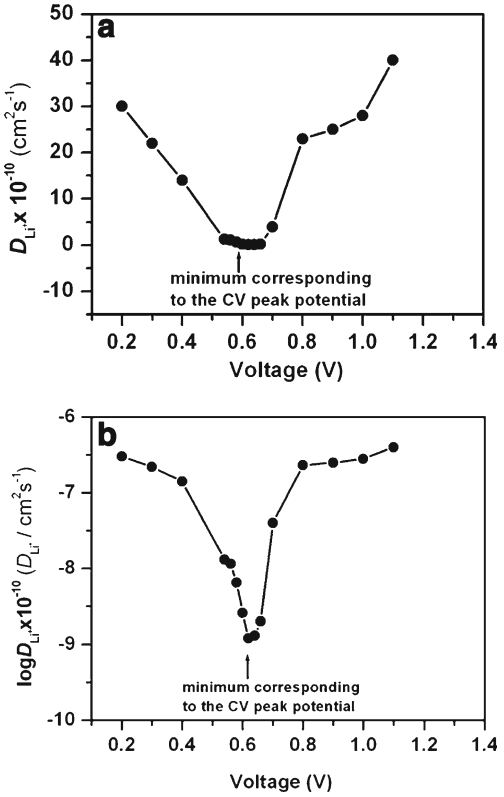

Fig. 11 Plots of **a** D_{Li+} and **b** log D_{Li+} against discharge voltage in 5 M $LiNO_3$ solution

1.2 V. Quantitatively all the spectra can be distinguished in these sections: a potential dependent semicircle in the high frequency region, a Warburg type element in the middle to low frequency region (straight line with 45° angle to Z' axis) and a steep sloping line at the lower frequencies. These impedance spectra reflect the nature of overall lithium ion de-intercalation process: the high frequency semicircle is related to charge transfer through the electrode/electrolyte interface, the Warburg region is assigned to solid state diffusion of lithium ions through the bulk of the electrode, while the steep sloping line reflects a capacitive behavior of the electrode [12]. Two types of current through the electrode–electrolyte interface can be distinguished: one due to lithium ion and electron migration (faradaic current), and the other due to displacement current because of charge polarization (non-faradaic current). These two currents flow in parallel branches. The faradaic current branch may be represented by charge transfer resistance R_{ct} and by Warburg impedance $Z_{w,}$ the non-faradaic current branch by a double layer capacitance C_{dl} [19].

The potential dependence of impedance spectra measured from intercalation electrodes can be conveniently presented and analyzed when coupled with the related potential dependence of intercalation capacitance (C_{int}) of the same electrode. C_{int} for lithium intercalated hosts is inversely proportional to the imaginary part of the impedance ($-Z''$) at very low frequencies ($\omega \rightarrow 0$), $C_{int}=(-\omega Z'')$, where ω is the angular velocity of the ac response. Thus ($-Z''$) measured at a sufficiently low frequency for a family of Nyquist plots at different potentials can be correlated with C_{int} measured, for example, by slow scan cyclic voltammetry (SSCV). The characteristic impedance spectra and its potential dependence provides important kinetic information on the mechanism of intercalation processes, which cannot be obtained from the C_{int} vs E plots [28–30]. Figure 4a shows a family of Nyquist plots related to lithium ion de-intercalation into the layered phase within the potential region I. The main

Table 2 Evaluated impedance parameters according to the equivalent circuit in Fig. 5b as a function of electrode potential during discharge process

E (V)	R_s (Ω)	R_{ct} (Ω)	(I_o/10^{-4}) (A)	C_{dl} (mF)	Z_w (Ω)	(D_{Li+}/10^{-10})/ cm^2 s^{-1}	log[(D_{Li+}/10^{-10})]/ cm^2 s^{-1}
1.10	0.726	53.28	3.21	1.180	0.0019	40.00	−6.397
1.00	0.716	80.9	3.17	1.060	0.0043	28.00	−6.552
0.90	0.711	99.1	2.59	1.005	0.0100	25.00	−6.602
0.80	0.692	126.1	2.04	0.952	0.0192	23.00	−6.638
0.70	0.666	184.1	1.40	0.722	0.0541	4.00	−7.397
0.66	0.669	206.8	1.24	0.630	0.1271	0.20	−8.698
0.64	0.680	250.4	1.03	0.491	0.0840	0.13	−8.886
0.62	0.683	293.1	0.88	0.442	0.0646	0.12	−8.920
0.60	0.682	343.0	0.75	0.415	0.0476	0.26	−8.585
0.58	0.688	394.7	0.65	0.399	0.0347	0.65	−8.187
0.56	0.688	421.5	0.61	0.395	0.0303	1.14	−7.942
0.54	0.687	451.7	0.57	0.392	0.0259	1.30	−7.886
0.40	0.666	792.6	0.32	0.528	0.0098	14.00	−6.853
0.30	0.653	881.1	0.39	0.586	0.0088	22.00	−6.657
0.20	0.657	932.2	0.28	0.606	0.0074	30.00	−6.522

feature of this region is that it exhibits semicircles (high frequency semicircle, HFS) which are not complete towards the low frequencies. The diameter of these arc shaped curves decreases with the increase in potential, followed by a sloping, low frequency capacitive line. Figure 4b shows the Nyquist plots in region II (i.e., during the beginning of de-intercalation). The diameter of the arc decreases further so that a semicircle rather than an arc appears with a decrease in the sloping capacitive behavior. Figure 4c shows the family of impedance spectra in the vicinity of CV peak potentials. In this domain the impedance spectra shows minimum with respect to $-Z''$ values with almost constant HFS diameters. The low frequency capacitive lines disappear completely and the Warburg behavior dominates the low frequency region of the spectra, as diffusion is the main process after high frequency relaxation. Figure 4d shows the impedance spectra measured in the domain IV, i.e., towards the end of lithium ion de-intercalation process. The HFS diameter increases as the potential becomes more positive towards the end of lithium de-intercalation process as evident from frequencies indicated in the figure. In Fig 4c, we see a curve with a minimum at 0.72 V when all the points related to the $-Z''$ values at 5 mHz, i.e. the lowest frequency used in this study are compared with each other. The potential of the above minimum corresponds to the potential of CV peak. Thus the low frequency impedance measurements are in qualitative agreement with the SSCV characterizations of the same electrode (i.e., the EIS data fulfill the condition $C_{int}=-(\omega Z'')^{-1}$ at $\omega \rightarrow 0$). A more quantitative comparison is not possible because of the quite different accessible time windows of the SSCV and EIS techniques used in this study [28].

Figure 5a shows the simulated curve during de-intercalation process at 0.70 V. In accordance with the results obtained an equivalent circuit, as shown in Fig. 5b, is proposed to fit the impedance spectra. In this equivalent circuit R_s represents the ohmic resistance of the electrolyte solution, R_{ct} is the resistance of the charge transfer reaction, Q is the capacitance of the electrode–electrolyte double layer, and Z_w is the Warburg impedance. To get better fitting results, pure capacitor in the equivalent circuit is replaced by constant phase element (CPE, Q). CPE is used when impedance spectra exhibits low frequency dispersion. It is suggested that such dispersion could be caused by the film–substrate interface, roughness, porosity, or in homogeneity [31]. A Nyquist plot of similar compounds in non aqueous electrolytes consists of two semicircles: a potential independent semicircle in the high frequency region and a strongly potential dependent larger semicircle in the medium frequency region [32]. The high frequency semicircle reflects the resistance for lithium ion migration through the surface film and film capacitance of the electrode. The absence of this region may be due to high rate performance (short diffusion path) and/or a small resistance offered by the surface layer for the migration of lithium ions which does not resist the diffusion of lithium ions.

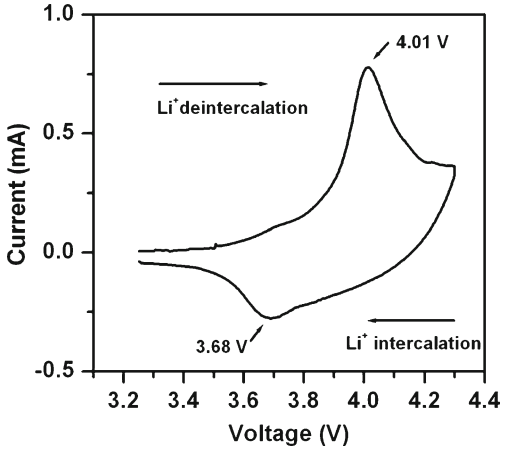

Fig. 12 Cyclic voltammetry of $LiNi_{1/3}Mn_{1/3}Co_{1/3}O_2$ electrode in 1 M $LiAsF_6$/EC+DMC at a scan rate of 0.05 mV s^{-1}

The values of the kinetic parameters calculated from the impedance data during the charge process are summarized in Table 1 and Fig. 6 shows the variation of kinetic parameters with applied potential. Solution resistance R_s stays constant at about 0.6 Ω as expected because solution composition and thus conductance do not change. R_{ct} decreases with the potential and reaches at a minimum at 0.74 V, and then increases (Fig. 6a). The Butler–Volmer equation can be linearized when the amplitude of the potential perturbation

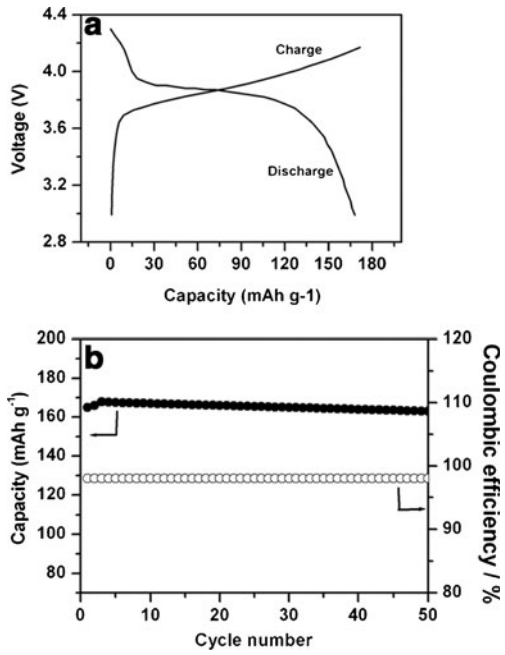

Fig. 13 **a** Charge–discharge curves **b** cycling stability and coulombic efficiency curves of Li/1 M $LiAsF_6$/EC+DMC/$LiNi1_{/3}Mn_{1/3}Co_{1/3}O_2$ cell at the current density of 0.1 mA cm^{-2}

signal is less than 10 mV [23]. The exchange current I_0 is calculated according to the following equation.

$$I_0 = RT/nFR_{ct} \quad (3)$$

Figure 6b shows the variation of I_0 with charge voltage. I_0 increases with the potential and reaches a maximum at 0.74 V, when the charge transfer resistance is lowest, and then decreases. From the CV curves, it can be seen that around 0.74 V the oxidation reaction shows a peak implying favorable kinetic conditions for de-intercalation.

C_{dl} decreases slightly at first with the voltage, perhaps due to a conceivable activation process since there is no passivating film on the surface of the electrode, and then increases (Fig. 6c). Since C_{dl} represents the double layer capacitance of the electrode–solution interface, it is a function of electrode potential and does not behave like a simple capacitor, whose capacity is independent of the applied voltage [23]. Z_w shows a maximum at 0.72 V, which corresponds to CV peak potential (Fig. 6d). When lithium ions de-intercalate into the layered structure, Z_w increases and then decrease subsequently. The diffusion coefficient of lithium ion, D_{Li+} can be determined from the impedance data by analyzing the low frequency Warburg contribution. The relation of D_{Li+} with the impedance response can be expressed as [13]

$$Z_w = V_m(dE/dx)/FA(2D)^{1/2} \quad (4)$$

Where V_m is the molar volume of $LiNi_{1/3}Mn_{1/3}Co_{1/3}O_2$, F is the Faraday constant, and Z_w is the Warburg coefficient, which

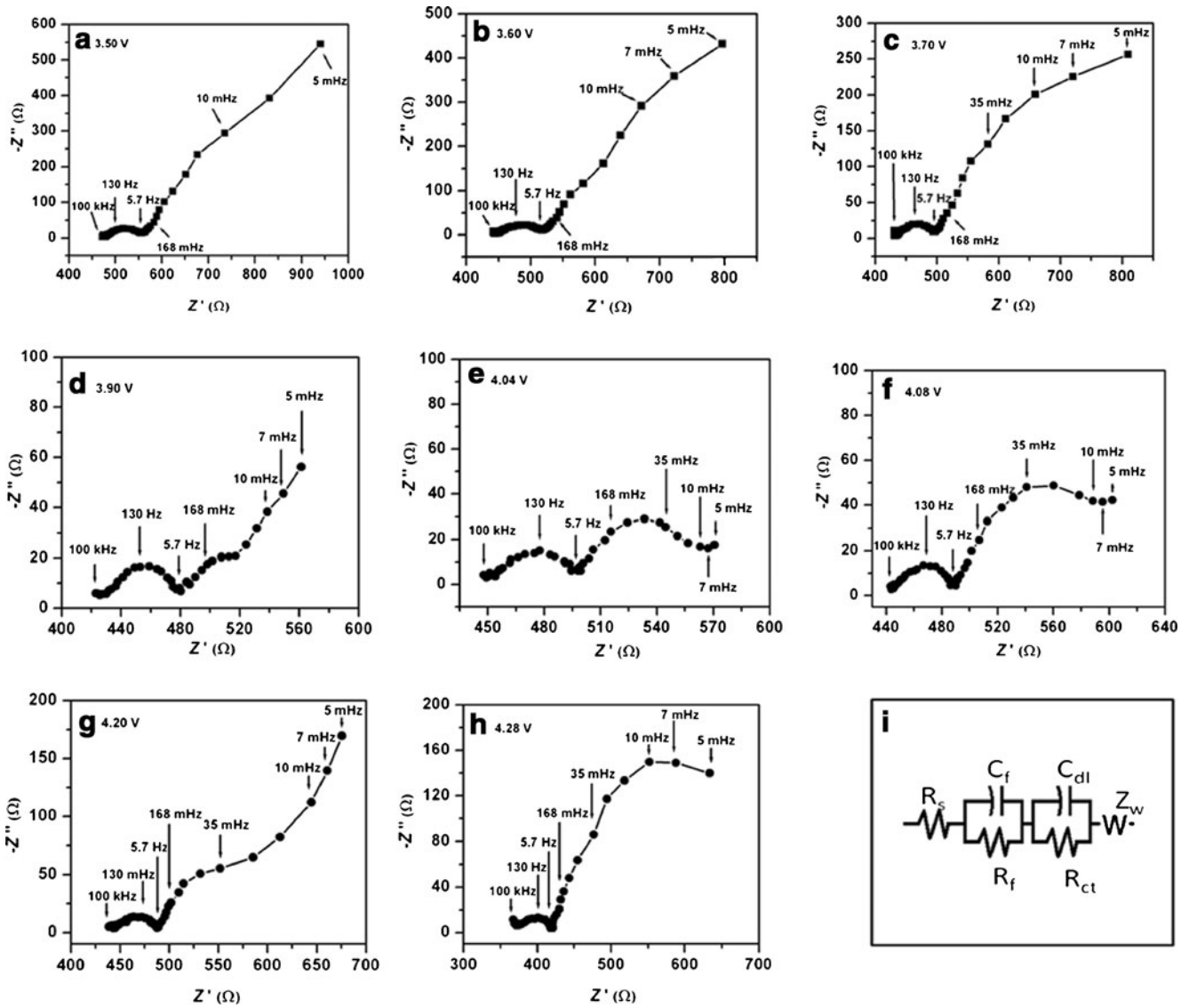

Fig. 14 Nyquist plots of the $LiNi_{1/3}Mn_{1/3}Co_{1/3}O_2$ electrode in 1 M $LiAsF_6$/EC+DMC at different charge voltages and simulated result obtained using the equivalent circuit in Fig. 12i

is obtained from simulation of the Warburg impedance spectra at low frequency. The dE/dx values are determined from the SSCV curve in Fig. 2, and A is the electrode surface area. Figure 7 shows the variation of D_{Li+}, calculated by using Eq. (4), with applied potential. It can be seen that the diffusion coefficient of lithium ion gradually decreases and reaches a minimum at a potential which corresponds to CV peak and then increases.

Intercalation of lithium ions into $LiNi_{1/3}Mn_{1/3}Co_{1/3}O_2$ layered phase from 5 M $LiNO_3$ solution was studied by EIS in the same manner as that of de-intercalation of the same electrode. Similar to the Nyquist plots for lithium ion de-intercalation the spectra for intercalation also contains a sloping, low frequency capacitive line, a Warburg element, and a HFS. Figure 8a shows a family of impedance spectra related to the potential domain I during intercalation of lithium ions. The HFS diameter increases with decrease in potential due to charge transfer reaction. When the $-Z''$ values are compared at the frequency of 5 mHz, it is clear that the sloping capacitive line decreases with decrease in potential. The low frequency capacitive line disappears as the potential approaches the CV peak potential indicating the beginning of intercalation. Figure 8b shows impedance spectra related to domain II. The diameter of HFS continues to increase, but the low frequency capacitive lines disappear and the Warburg behavior dominates the low frequency region of all the spectra in this domain. Figure 8c covers the impedance spectra of the electrode related to domain III (i.e., along the CV peak). In this region a small change in HFS diameter is observed. The low frequency sloping capacitive line appears again in this domain indicating a semi-infinite diffusion of lithium ions in the solid state. Figure 8d relates to the potential domain IV, where the diameter of the semicircle is almost independent of the potential applied as the charge transfer process is absent at the end of intercalation. The low frequency capacitive lines become more predominant in this domain.

The simulation of equivalent circuit to the impedance spectra data measured at the potential corresponding to the CV peak potential during intercalation is shown in Fig. 9. Good fitting results were obtained for all the spectra using the same equivalent circuit.

Figure 10 shows the variation of kinetic parameters of the equivalent circuit from the experimental impedance data of the $LiNi_{1/3}Mn_{1/3}Co_{1/3}O_2$ electrode with the decrease of the potential. R_s stay constant with decreasing potential as expected. From Fig. 10a, it can be seen that R_{ct} increased when the potential shifts in the negative direction. Correspondingly, I_0 decreases with the decrease in potential (Fig. 10b). This is because a higher potential would imply favorable kinetic condition for intercalation. Such a behavior is reported for $LiMn_2O_4$ in non-aqueous electrolyte [13]. Figure 10c shows C_{dl}=1.2 mF at the beginning and then decreases with the negative shift of the potential. The C_{dl}

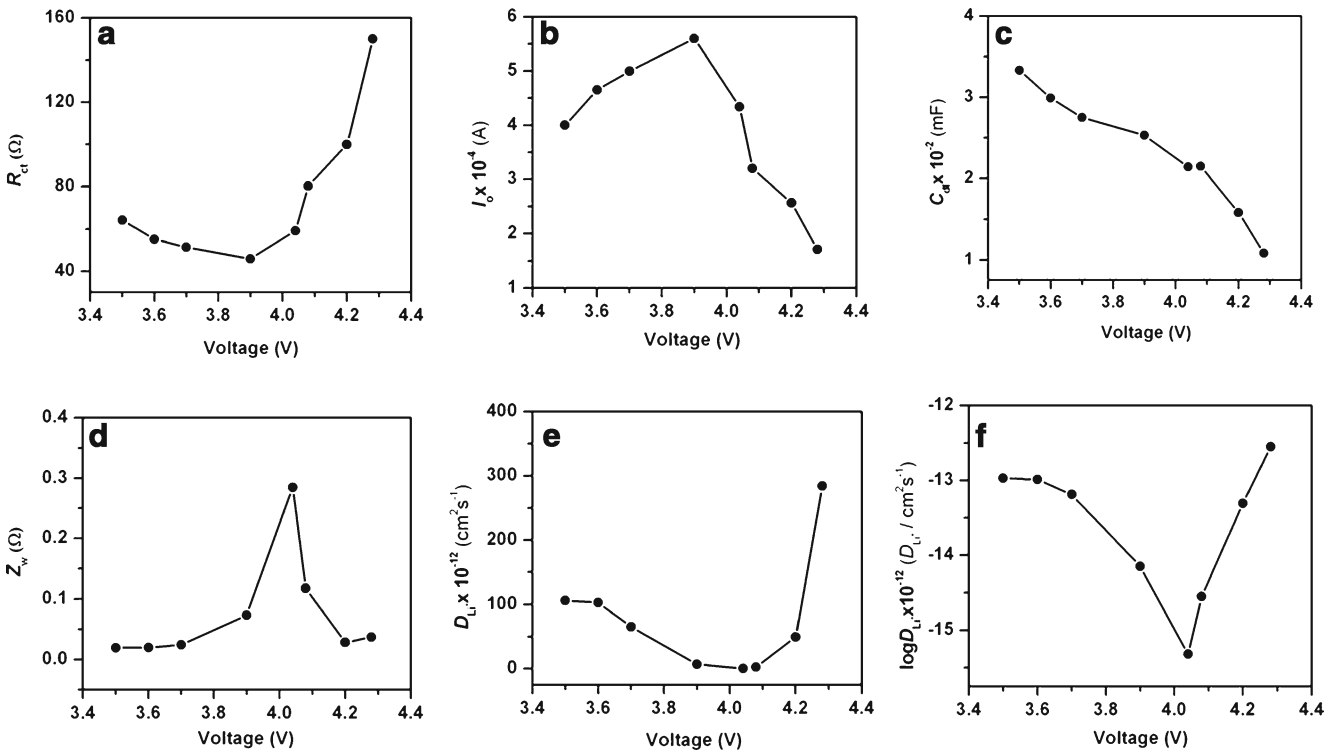

Fig. 15 Relationship between kinetic parameters and charge voltage in 1 M $LiAsF_6$/EC+DMC

decreases gradually during the intercalation of lithium ions and then reaches to the minimum at the potential corresponding to the CV peak (0.56 V). Subsequently the value of C_{dl} increases gradually to a maximum value. As the potential decrease, Z_w increases gradually and reaches a maximum near the potential where the intercalation is maximum and then decreases (Fig. 10d). Figure 11 shows the variation of D_{Li+} with discharge potential. The D_{Li+} value decreases and shows a minimum at potential close to CV peak potential. This is due to the fact that, at the lithium rich-state, the incoming lithium ions have to overcome repulsive interactions with those located at the inserted sites. For the lithium ion diffusion channel to be available, the lithium ions located at inserted sites have to hop and occupy their nearest neighbor and empty their sites, accompanied by the breakdown of old Li–O bonds and the formation of new Li–O bonds. The applied potential is responsible for the breakdown of Li–O bonds. The values of kinetic parameters measured during discharge are as shown in Table 2.

Figure 12 shows the CV profile of $LiNi_{1/3}Mn_{1/3}Co_{1/3}O_2$ obtained in the organic electrolyte at a scan rate of 0.05 mV s^{-1}. The cell was cycled in the range of 3.0–4.3 V (vs. Li/Li^+). A pair of redox peaks at 4.01 and 3.68 V which correspond to the lithium ion de-intercalation/intercalation are observed. It can be seen clearly that in the non-aqueous solution the current response of the redox reaction is much lower than in the aqueous electrolyte solution due to slow charge transfer process. The solvation of lithium ions in the organic solvent with high dipole moment and the resistance offered by the surface layer for lithium ion migration will have a retardation effect on the kinetics of lithium ion insertion. Furthermore, it can be seen that the electrode polarization

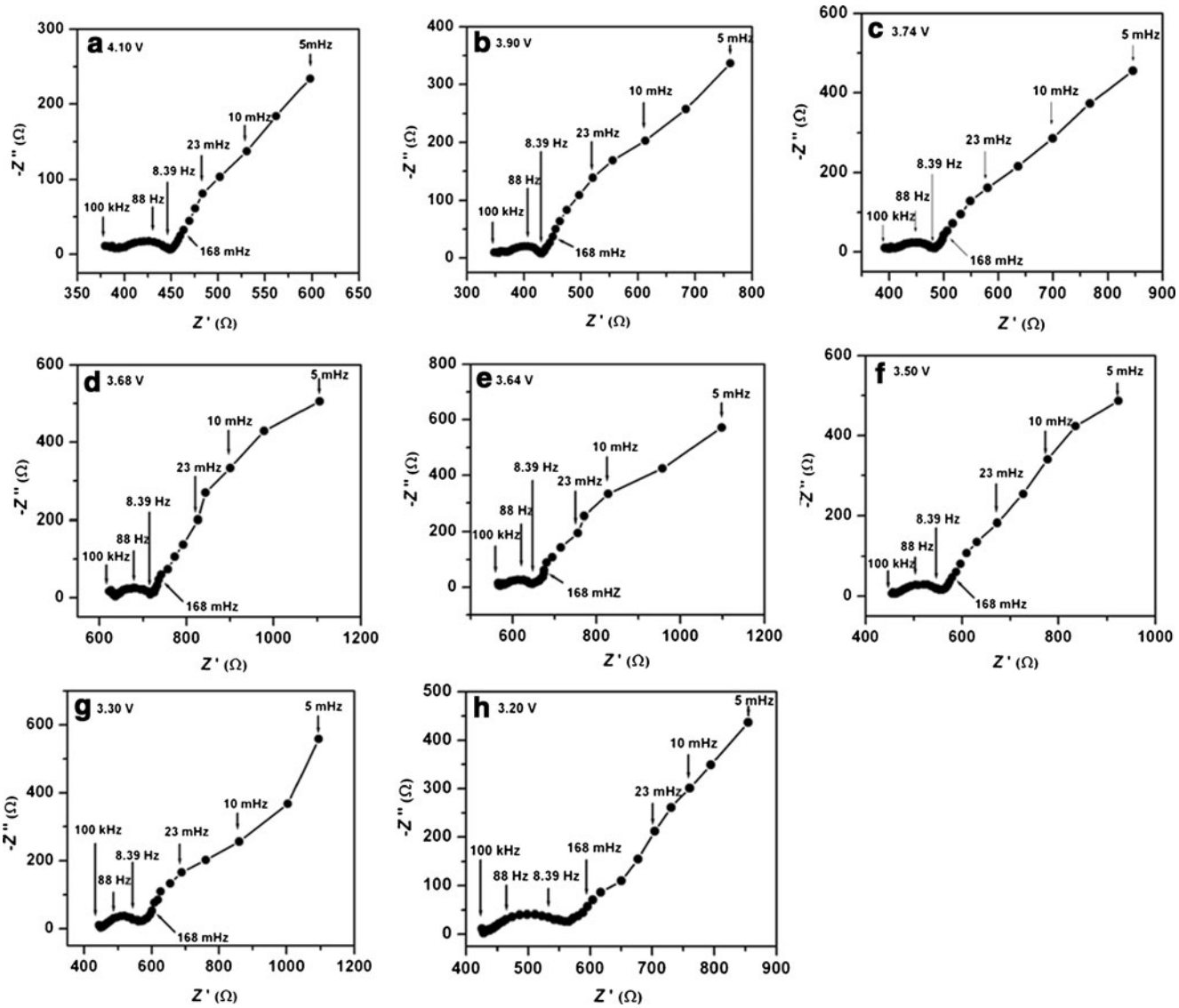

Fig. 16 Nyquist plots of the $LiNi_{1/3}Mn_{1/3}Co_{1/3}O_2$ electrode in 1 M $LiAsF_6$/EC+DMC at different discharge voltages

increases significantly in the organic electrolyte so that the shoulder-like peaks overlap with each other and are less pronounced. In the aqueous solution (Fig. 2) the smaller peaks appear due to the low electrode polarization.

Figure 13 shows the charge–discharge and cycling stability curves of Li/1 M $LiAsF_6$/EC+DMC/$LiNi1_{/3}Mn_{1/3}Co_{1/3}O_2$ cell at the current density 0.1 mA cm^{-2} in the potential range 3 to 4.3 V. the curves are similar to that in aqueous electrolyte (Fig. 3), except that the capacity in the former is lower than that in the latter. This result clearly shows that the charge and discharge behavior in organic electrolytes can be compared with the aqueous solution if the intercalation and de-intercalation voltages are within the stable electrochemical window of water.

Figures 14a–h shows Nyquist plots obtained from the $LiNi_{1/3}Mn_{1/3}Co_{1/3}O_2$ electrode in the organic electrolyte at different applied potentials during the charge process. Comparing the EIS responses (Fig. 4 and Fig. 14) of the electrode to an applied potential, it is clearly seen that the solution resistance, R_s is higher for organic electrolyte than that obtained with aqueous electrolyte. This once again suggests the low ionic conductivity of the organic electrolyte in accordance with the CV studies of the same electrode in aqueous and non-aqueous electrolytes. The Nyquist plots consists of three parts : a potential independent semicircle in the high frequency region (HFS), a potential-dependent larger semicircle in the medium-frequency region (MFS), a Warburg type element in the low-frequency region, and a steep sloping line at the lower frequencies. The high frequency semicircle is related to lithium ion migration through the surface film of the electrode, the medium frequency semicircle is related to charge-transfer through the electrode-electrolyte interface, the Warburg region is assigned to solid state diffusion of lithium ion through the electrode, while the steep sloping line reflects a capacitive behavior that is related to the occupation of lithium ion in insertion sites.

As expected, the diameter of the HFS remains constant as it is potential independent. However, the diameter of the MFS change during charging as this correspond charge-transfer process which is strongly potential dependent. Initially the charge-transfer resistance is so large that the MFS is hardly seen (Fig. 14a–c). However, as the potential approaches the CV peak potential, the charge-transfer resistance decreases and MFS is clearly seen (Fig. 14d–f). When all points related to $-Z''$ values are compared at 5 mHz, the lowest frequency used in this measurement, it shows a minimum at 4.04 V. This potential corresponds to the vicinity of CV peak during charge. Figure 14g–h represents the EIS response of the electrode in the highly de-lithiated state (end of de-intercalation). These spectra show reverse development with potential as compared to the initial stages of de-intercalation. The increase of the diameter of the middle frequency semicircle with the shift of potential towards more positive values is pronounced. It can be seen that throughout the de-intercalation process the diameter of the

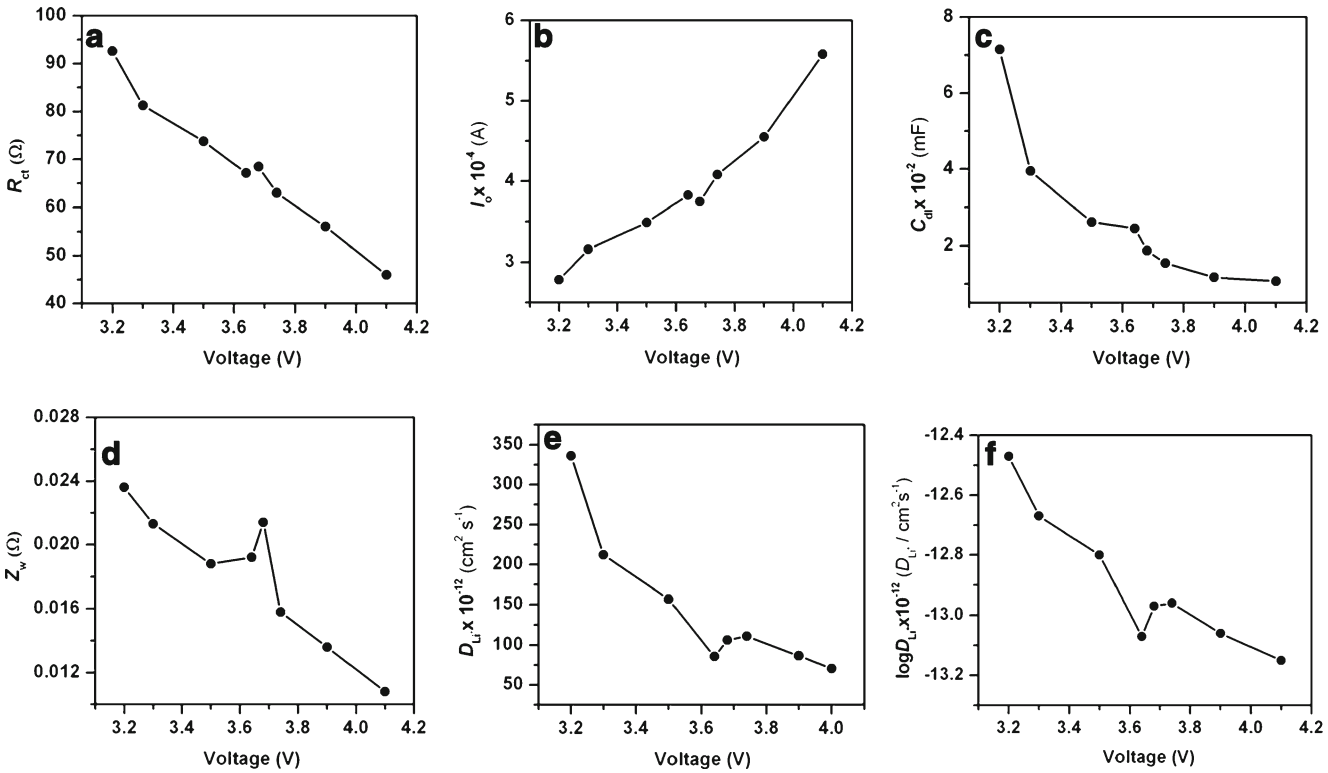

Fig. 17 Relationship between kinetic parameters and discharge voltage in 1 M $LiAsF_6$/EC+DMC

high frequency semicircle is practically independent of the potential applied as the surface film capacitance and the resistance for lithium ion migration through the surface film do not vary much with the potential. The capacitance value calculated from the maxima of the imaginary component of the semicircle and the potential dependence of the diameter of the medium frequency semicircle can be assigned to electronic and ionic charge transfer across the current collector/host and host/solution interfaces, respectively. The appearance of a pronounced medium frequency semicircle during the de-intercalation potentials (Fig. 14d–f) can be assigned to the charge-transfer through the double layer, which is a maximum at these potentials. According to the results obtained, an equivalent circuit, as shown in Fig. 14i, is proposed to fit the impedance spectra and the kinetic parameters were obtained by simulating the experimental data. In the equivalent circuit, C_f represents the surface film capacitance, R_f the resistance for lithium ion migration through the surface film, R_{ct} charge-transfer resistance at the bulk-electrolyte interface, C_{dl} double layer capacitance, and Z_w the Warburg impedance.

Figure 15 shows the variation of kinetic parameters with potential obtained by evaluating the experimental EIS data with the equivalent circuit. Variation of R_s, R_{ct}, I_0, and Z_w exhibits the same trend with the applied potential as observed with aqueous electrolytes during charge (Fig. 6). The C_{dl} shows a different trend in organic electrolyte. Such a variation in C_{dl} with applied potential during lithium de-intercalation has been reported [14]. The important kinetic parameter D_{Li+} decreases with potential and it reaches a minimum at 4.04 V which correspond to the vicinity of CV peak potential and then it increases towards the end of lithium de-intercalation. Further, the D_{Li+} values of lithium ions in aqueous and non-aqueous electrolytes are close to each other. This shows that the diffusion of lithium ions does not change much since the $LiNi_{1/3}Mn_{1/3}Co_{1/3}O_2$ host is the same and the diffusion happens in the solid phase.

Figure 16 shows the Nyquist plots obtained at different potentials during lithium ion intercalation. All the spectra exhibit the same trend as discussed earlier in the case of aqueous electrolyte during discharge (Fig. 8). The diameter of the MFS is lowest at 3.68 V, which corresponds to CV peak potential during discharge. The kinetic parameters also show a similar variation with decrease in potential (Fig. 17). Chemical diffusion coefficient, D_{Li+} shows minima at the potential which correspond to the CV peak potential.

Conclusion

Measurements of electrochemical impedance spectroscopy of $LiNi_{1/3}Mn_{1/3}Co_{1/3}O_2$ in aqueous and organic solutions shows that the mechanism of intercalation and de-intercalation of lithium ions are similar to that reported for other layered intercalation materials. The EIS technique complements the less resolved technique such as CV which does not provide insight into fast stages of intercalation/de-intercalation mechanism. The kinetic parameters of lithium ion intercalation/de-intercalation of $LiNi_{1/3}Mn_{1/3}Co_{1/3}O_2$ electrode in both the electrolytes vary with potential. It is found that the diffusion coefficient of lithium ions obtained in the aqueous electrolyte is close to that obtained with the organic electrolyte. This is in agreement with the fact that the diffusion of lithium ions occurs in the solid bulk of the electrode material and the nature of electrolyte is less likely to affect the process as the electrons does not exist inside the bulk of electrode material. These results encourage further research on safe and reliable use of $LiNi_{1/3}Mn_{1/3}Co_{1/3}O_2$ as a cathode material for aqueous rechargeable lithium batteries.

Acknowledgments Financial support from the Department of Science and Technology, Government of India is greatly acknowledged. The authors gratefully thank Sri. A. V. S. Murthy, honorary secretary, Rastreeya Sikshana Samiti Trust, Bangalore and Dr. P. Yashoda, Principal, S.S.M.R.V. Degree College, for their continuous support and encouragement. Department of Chemistry, St. Joseph's College, Bangalore, is acknowledged for XRD experimental support. We are greatfull to Prof. Munichandraiah, Inorganic and physical chemistry division, Indian Institute of Science, Bangalore for helping us to carryout experiment in non aqueous electrolytes.

References

1. Li W, Dahn JR, Wainright DS (1994) Science 264:1115–1118
2. Wang H, Huang H, Zeng Y, Zhao F, Chem L (2007) Elctrochem Solid State Lett 10(9):A119–A203
3. Manjunatha H, Suresh GS, Venkatesha TV (2010) J Solid State Electrochem 15(3):431–445
4. Reimers JN, Dahn JR (1992) J Electrochem Soc 139:2091–2097
5. Ozhuku T, Makimura Y (2001) Chem Lett 30:642–643
6. Li DC, Muta T, Zhang LQ, Yoshio M, Noguchi H (2004) J Power Sources 132:150–155
7. Yabuuchi N, Ozhuku T (2003) J Power Sources 171:119–121
8. Shaju KM, Subba Rao GV, Choudari BVR (2002) Electrochim Acta 48:145–151
9. Belharouak I, Sun YK, Li J, Amine K (2003) J Power Sources 123:247–252
10. Nukuda T, Inamasu T, Fujii A, Endo D, Nakagava H, Kosono S, Iguchi T, Kuratomi J, Kohono K, Izuchi S, Oshitani M (2005) J Power Sources 146:611–616
11. Wang ZX, Sun YC, Chen LQ, Huang XJ (2004) J Electrochem Soc 151:A914–A921
12. Choi J, Manthiram A (2004) Electrochem Solid State Lett 7:A365–A367
13. Chung, Lu H, Lin YK (2009) J Power Sources 189:40–44
14. Lu D, Li W, Zuo X, Yuan Z, Huang Q (2007) J Phys Chem C 111:12067–12074
15. Nobili F, Tossici T, Marassi R, Crocee F, Scrosati B (2002) J Phys Chem B 106:3909–3915
16. Bueno PR, Leite ER (2003) J Phys Chem B 107:8868–8877
17. Levi MD, Salitra G, Markovsky B, Teller H, Aurbach D, Heider U, Heider L (1999) J Electrochem Soc 146:1279–1289

18. Aurbach D, Levi MD, Teller H, Markovsky B, Salitry G (1998) J Electrochem Soc 145:3024–3034
19. Mohamedi M, Makino M, Dokko K, Itoh T, Uchida I (2002) Electrochim Acta 48:79–84
20. Stiebel KA, Sakai E, Cairns EJ (2002) J Electrochem Soc 149: A61–A68
21. Thomas MGSR, Bruce PG, Goodenough JB (1985) J Electrochem Soc 132:1521–1528
22. Shalini R, Munichandraiah N, Shukla AK (2000) J Power Sources 87:12–20
23. Sinha NN, Ragupathy P, Vasan HN, Munichandraiah N (2008) Int J Electrochem Sci 3:691–710
24. Wang GJ, Qu QT, Wang B, Shi Y, Tian S, Wu YP, Holze R (2009) Electrochim Acta 54:1199–1203
25. Manjunatha H, Mahesh KC, Suresh GS, Venkatesha TV (2011) Electrochim Acta 56:1439–1446
26. Wan H, Huang K, Zeng Y, Zhao F, Chen L (2007) Electrochem Solid State Lett 10:A199–A203
27. Wang GJ, Fu LJ, Wang B, Zhao NH, Wu YP, Holze R (2008) J Appl Electrochem 38:579–581
28. Levi MD, Gizhar H, Lancry E, Gofer Y, Levi E, Aurbach D (2004) J Electroanal Chem 569:211–223
29. Levi MD, Aurbach D (1997) J Phys Chem B 101:4641–4647
30. Levi MD, Aurbach D (1999) Electrochim Acta 45:167–185
31. Ho C, Raistriek ID, Huggins RA (1980) J Electrochem Soc 127:343–350
32. Lin B, When Z, Gu Z, Huang S (2008) J Power Sources 175:564–569